



Article

# Functionalized Ultrasmall Iron Oxide Nanoparticles for $T_1$ -Weighted Magnetic Resonance Imaging of Tumor Hypoxia

Lei Yang<sup>1</sup>, Mohammad Javad Afshari<sup>2</sup> , Jianxian Ge<sup>2</sup>, Dandan Kou<sup>2</sup>, Lei Chen<sup>2</sup> , Dandan Zhou<sup>2</sup>, Cang Li<sup>2</sup>, Shuwang Wu<sup>2</sup>, Leshuai Zhang<sup>2</sup>, Jianfeng Zeng<sup>2,\*</sup>, Jian Zhong<sup>1</sup>, Roland H. Stauber<sup>3</sup> and Mingyuan Gao<sup>1,2,\*</sup>

<sup>1</sup> College of Food Science & Technology, Shanghai Ocean University, Shanghai 201306, China

<sup>2</sup> Center for Molecular Imaging and Nuclear Medicine, State Key Laboratory of Radiation Medicine and Protection, School for Radiological and Interdisciplinary Sciences (RAD-X), Collaborative Innovation Center of Radiological Medicine of Jiangsu Higher Education Institutions, Soochow University, Suzhou 215123, China

<sup>3</sup> Department of Nanobiomedicine, ENT, University Medical Center of Mainz, Langenbeckstr. 1, 55101 Mainz, Germany

\* Correspondence: jfzeng@suda.edu.cn (J.Z.); gaomy@iccas.ac.cn (M.G.)

**Abstract:** Hypoxia is a common biological condition in many malignant solid tumors that plays an imperative role in regulating tumor growth and impacting the treatment's therapeutic effect. Therefore, the hypoxia assessment is of great significance in predicting tumor development and evaluating its prognosis. Among the plenty of existing tumor diagnosis techniques, magnetic resonance imaging (MRI) offers certain distinctive features, such as being free of ionizing radiation and providing images with a high spatial resolution. In this study, we develop a fluorescent traceable and hypoxia-sensitive  $T_1$ -weighted MRI probe (Fe<sub>3</sub>O<sub>4</sub>-Met-Cy5.5) via conjugating notable hypoxia-sensitive metronidazole moiety and Cy5.5 dye with ultrasmall iron oxide (Fe<sub>3</sub>O<sub>4</sub>) nanoparticles. The results of in vitro and in vivo experiments show that Fe<sub>3</sub>O<sub>4</sub>-Met-Cy5.5 has excellent performance in relaxivity, biocompatibility, and hypoxia specificity. More importantly, the obvious signal enhancement in hypoxic areas indicates that the probe has great feasibility for sensing tumor hypoxia via  $T_1$ -weighted MRI. These promising results may unlock the potential of Fe<sub>3</sub>O<sub>4</sub> nanoparticles as  $T_1$ -weighted contrast agents for the development of clinical hypoxia probes.

**Keywords:** tumor hypoxia; ultrasmall iron oxide nanoparticles; magnetic resonance imaging; metronidazole



**Citation:** Yang, L.; Afshari, M.J.; Ge, J.; Kou, D.; Chen, L.; Zhou, D.; Li, C.; Wu, S.; Zhang, L.; Zeng, J.; et al. Functionalized Ultrasmall Iron Oxide Nanoparticles for  $T_1$ -Weighted Magnetic Resonance Imaging of Tumor Hypoxia. *Molecules* **2022**, *27*, 6929. <https://doi.org/10.3390/molecules27206929>

Academic Editor: Krishan Kumar

Received: 1 September 2022

Accepted: 12 October 2022

Published: 15 October 2022

**Publisher's Note:** MDPI stays neutral with regard to jurisdictional claims in published maps and institutional affiliations.



**Copyright:** © 2022 by the authors. Licensee MDPI, Basel, Switzerland. This article is an open access article distributed under the terms and conditions of the Creative Commons Attribution (CC BY) license (<https://creativecommons.org/licenses/by/4.0/>).

## 1. Introduction

The tumor microenvironment (TME), closely related to the tumor growth and metastasis [1], is often a starting point for the study of tumor development and pathological processes. During the expansion of a tumor, the tumorous tissues located far from the blood vessels might encounter a state of oxygen deficiency (i.e., hypoxia) as a consequence of the imbalance between the oxygen supply capacity and the consumption rate [2,3]. Hypoxia is an important characteristic of many pathological parameters (low pH, abnormal expression of enzymes) in TME, which greatly affects the prognosis and treatment of tumors [4–6]. The incidence of hypoxia in most advanced solid tumors and its capability to activate hypoxia-inducible factor-1 $\alpha$  (HIF-1 $\alpha$ ) have been previously confirmed [7,8]. The factor can promote the invasion and metastasis of tumor cells, as well as a greater tolerance to radio- and chemotherapy [9,10]. Therefore, predicting tumor hypoxia and visualizing its distribution is of great significance for the formulation of tumor treatment protocols and the evaluation of prognosis.

Compared with the traditional oxygen electrode method [11,12], the molecular imaging technique, which can detect tumor hypoxia, is becoming more prevalent recently for its non-invasive and real-time imaging characteristics [13–15]. In particular, optical imaging

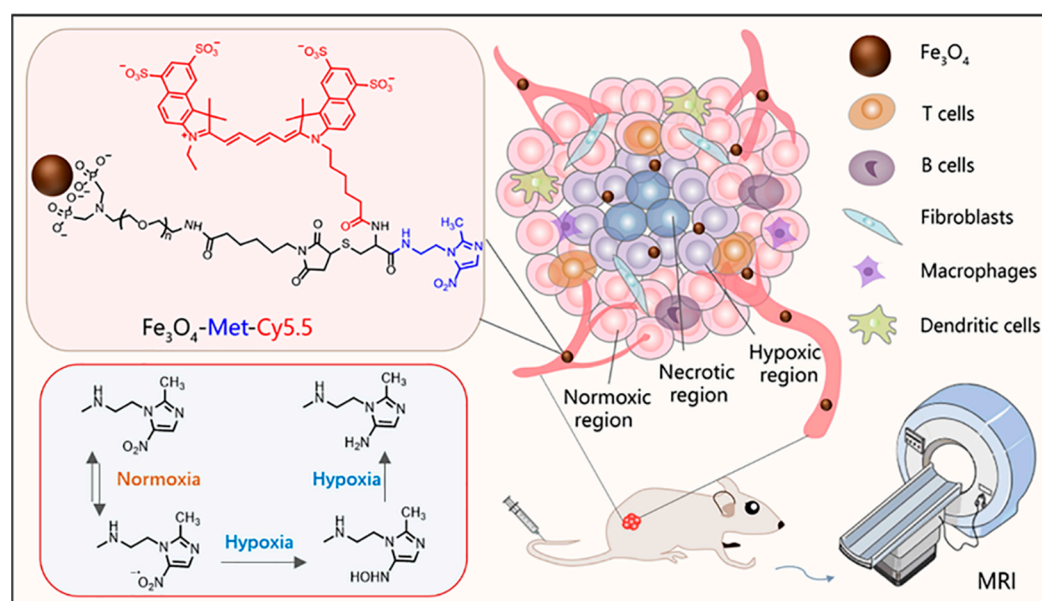
and nuclear medicine imaging have contributed a lot to this research. In optical imaging, hypoxia fluorescent probes mostly connect dye molecules with sensitive moieties, such as nitroimidazole and azobenzene, to quench the original fluorescence until the structure of the sensitive moieties is changed by related reductase under hypoxic conditions [16]. Apart from these probes, it has been found that some phosphorescence dyes, such as the ruthenium(II) and iridium(III) complexes, can also achieve the accurate sensing of O<sub>2</sub> content, according to the quenching degree of phosphorescence under different oxygen concentrations [17–19]. For example, our team previously reported a ratiometric O<sub>2</sub> sensing probe, which innovatively encapsulated the common hydrophobic oxygen-sensitive iridium(III) complex into β-cyclodextrin and then combined it with the oxygen-insensitive Cyanine7 dye [20]. This kind of design not only improves the water solubility and oxygen sensing sensitivity of the iridium(III) complex, but also successfully realizes the rapid and quantitative visualization of hypoxic regions in vivo. Although optical imaging has superiority in resolution and sensitivity, its spatial resolution and signal intensity declines significantly with the increase of tissue depth, thus leading to limitations in deeper tissue imaging of tumors.

However, nuclear medicine imaging is free of the aforementioned limitations and displays a greater advantage in clinical application. The most deserved to be mentioned is <sup>18</sup>F-fluoromisonidazole (<sup>18</sup>F-FMISO), which is widely used in clinical hypoxic research. It can evaluate the degree of tumor hypoxia, according to the relative signal enhancement caused by the selective accumulation in hypoxic cells [21]. Then, based on the mechanism of <sup>18</sup>F-FMISO, the researchers developed a series of improved probes, such as <sup>18</sup>F-fluoroazomycinarabinofuranoside (<sup>18</sup>F-FAZA) and <sup>18</sup>F-3-fluoro-2-(4-((2-nitro-1H-imidazol-1-yl)methyl)-1H-1,2,3-triazol-1-yl)propan-1-ol (<sup>18</sup>F-HX4) [22,23], which not only increase the water solubility, but also enhance the clearance rate and signal contrast. Despite this, nuclear medicine imaging is limited by low spatial resolution, thus leading to a lack of clarity in the distribution of tumor hypoxia.

Compared with the aforementioned methods, magnetic resonance imaging (MRI) has a better promising future in clearly depicting the hypoxia distribution because of its high spatial resolution and lack of limitation in tissue depth [24]. At present, Fe<sub>3</sub>O<sub>4</sub> nanoparticles have been developed as an alternative MRI contrast agent with excellent magnetic properties and biocompatibility [25] and have gradually become an outstanding carrier for the construction of tumor hypoxia probes in recent years. For instance, Filippi et al. developed a hypoxia-specific T<sub>2</sub>-weighted MRI probe by conjugating 10 nm-sized Fe<sub>3</sub>O<sub>4</sub> nanoparticles with the oxygen-sensitive metronidazole ligands and demonstrated its capability of selective accumulation into the hypoxic two-dimensional (2D) and three-dimensional (3D) cell models [26]. In addition, Zhou et al. constructed a hypoxia-triggered T<sub>2</sub>-weighted MRI probe by simultaneously modifying nitroimidazole and cysteine to the surface of Fe<sub>3</sub>O<sub>4</sub> nanoparticles [27]. Under the hypoxic environment, the bioreductions of the nitro group can subsequently form reductive adducts with the thiol group of cysteine on Fe<sub>3</sub>O<sub>4</sub> nanoparticles, thus cross-linking the nanoparticles to form larger assemblies and amplifying the T<sub>2</sub>-weighted MRI signal for the tumor interior region. Although these Fe<sub>3</sub>O<sub>4</sub>-based hypoxia probes exhibited splendid hypoxia selectivity, this mode highlights the lesion areas by a signal decline (darker images), which has been reported to affect the identification of tumors from internal bleeding, calcification, and metal deposition [28,29]. On the contrary, T<sub>1</sub>-weighted MRI is a way to brighten the regions of interest by an increase in signal (using T<sub>1</sub>-weighted images) intensity, which is intrinsically more sensitive than a decrease in signal (using T<sub>2</sub>-weighted images) intensity presented by T<sub>2</sub>-weighted MRI for reducing the impact on diagnostic accuracy. From this point of view, T<sub>1</sub>-weighted magnetic resonance imaging will have a better application prospect in the field of tumor hypoxia detection.

According to the report, Fe<sub>3</sub>O<sub>4</sub> nanoparticles can also be used as T<sub>1</sub>-weighted contrast agents when the core diameter is less than 5 nm [30–33]. Herein, to realize the T<sub>1</sub>-weighted MRI of tumor hypoxia, as shown in Scheme 1, ultras-small PEGylated Fe<sub>3</sub>O<sub>4</sub> nanoparticles

were synthesized and further conjugated with metronidazole and Cy5.5 fluorescent dye to construct a  $T_1$ -weighted MRI nanoprobe ( $\text{Fe}_3\text{O}_4$ -Met-Cy5.5). Firstly, the nanoprobe reaches the tumor tissue through the endothelial permeability and retention effect (EPR). Then, the nitro groups on the surface of nanoprobe will undergo a series of reduction reactions to form amino compounds under the action of reductase in hypoxic cells [34,35]. Finally, the compounds would eventually form bonds with macromolecular substances existing in the hypoxic regions [36], producing specific retention in hypoxia regions. Both the cellular evaluation and tumor imaging studies have proven that the  $\text{Fe}_3\text{O}_4$ -Met-Cy5.5 probe has excellent hypoxia sensitivity and can achieve a great  $T_1$ -weighted MRI of hypoxic tumors in vivo.



**Scheme 1.** The illustration of the  $\text{Fe}_3\text{O}_4$ -Met-Cy5.5 nanoprobe for in vivo  $T_1$ -weighted MRI and the mechanism of metronidazole trapped in hypoxic regions.

## 2. Materials and Methods

### 2.1. Materials

Iron(III) acetylacetonate ( $\text{Fe}(\text{acac})_3$ ), oleic acid, oleylamine, cyclohexane, N-hydroxysuccinimide (NHS), D-cysteine hydrochloride monohydrate (Cys), and Cy5.5-NHS ester were purchased from Aladdin. Tetrahydrofuran (THF) and acetone was purchased from Sinopharm Chemical Reagent Co., LTD., Shanghai, China. The 1-ethyl-3-(3-dimethylaminopropyl) carbodiimide hydrochloride (EDC) was purchased from Energy Chemical. Polyethylene glycol ( $M_w \approx 2000$  Da) with a diphosphate group at one end and a maleimide group at the other end, denoted as DP-PEG-Mal, was provided by Suzhou Xinying Biomedical Technology Co., LTD., Suzhou, China. Boc-Cys(Trt)-OH was purchased from Shanghai Maclin Biochemical Technology Co., LTD., Shanghai, China. The 1-(2-Aminoethyl)-2-methyl-5-nitroimidazolidihydrochloride was purchased from Acros Organics. Triethylsilane was purchased from TCI. Dulbecco's modified eagle medium (DMEM) and fetal bovine serum (FBS) were purchased from HyClone. Hoechst 33342 reagent was purchased from Beyotime Biotech. HIF-1 $\alpha$  mouse monoclonal antibody was purchased from Affinity.

### 2.2. Cells and Animals

Human breast cancer cells (MCF-7) were cultured in high glucose DMEM medium supplemented with 10% fetal bovine serum and 1% penicillin-streptomycin solution. The normoxic MCF-7 cells were cultured under the condition of 37 °C, 21%  $\text{O}_2$ , 5%  $\text{CO}_2$ , and 95% humid air in a carbon dioxide incubator. The hypoxic cells were cultured in a three-gas

incubator with low oxygen concentration. SPF nude mice (female, 4–5 weeks, weight of 18–20 g) were purchased from Changzhou Cavens Experimental Animal Co., Ltd., Changzhou, China. All animal experiments were approved by the Laboratory Animal Center of Soochow University. The subcutaneous tumor models were established by injecting MCF-7 cells ( $4 \times 10^6$  each) into the dorsal area near the right hind limb of each mouse.

### 2.3. Synthesis of Hypoxia-Sensitive Ligand (Met)

Boc-Cys(Trt)-OH (231.8 mg, 0.5 mmol), EDC (134.2 mg, 0.7 mmol), and NHS (135.8 mg, 1.18 mmol) were dissolved in  $\text{CH}_2\text{Cl}_2$  (5 mL), stirring for 20 min at room temperature under the atmosphere of nitrogen. The mixture solution of dimethylformamide (DMF) and N-diisopropylethylamine (DIPEA) containing 1-(2-Aminoethyl)-2-methyl-5-nitroimidazoledihydrochloride (170 mg, 0.65 mmol) was slowly injected into the above solution by a syringe, under the condition of ice bath, and stirred at room temperature overnight. After the reaction,  $\text{CH}_2\text{Cl}_2$  and DMF were evaporated by decompression rotation and freeze-dried to fully remove the liquid from the system. The yellow solid was extracted with saturated sodium bicarbonate solution three times. The organic phase was collected and dried with anhydrous sodium sulfate. After filtering and evaporating, the compound BM was further purified by Elite P3500 semi-preparative liquid chromatographic system.

The purified product BM (120 mg, 0.195 mmol) was dissolved in  $\text{CH}_2\text{Cl}_2$  and dripped with trifluoroacetic acid (TFA) and triethylsilane. The final product, Met, was purified by Elite P3500 semi-preparative liquid chromatographic system after the solvent was removed under reduced pressure.

### 2.4. Synthesis of Ultrasmall $\text{Fe}_3\text{O}_4$ Nanoparticles

Ultrasmall iron oxide nanoparticles ( $\text{Fe}_3\text{O}_4$ ) were prepared according to a previous report on a flow synthesis system [37]. Typically,  $\text{Fe}(\text{acac})_3$  (7.1 g, 20 mmol), oleic acid (38.7 g, 137 mmol), and oleylamine (36.6 g, 137 mmol) were dissolved in 0.9 L methylbenzene to prepare a flow reaction solution. The flowing reaction liquid was pumped into the tubular reactor by a high-pressure constant current pump. And the flow rate, temperature, and residence time were  $30 \text{ mL min}^{-1}$ ,  $270 \text{ }^\circ\text{C}$ , and 6 min. After that, the solution was cooled to room temperature and collected in sample bottles. Then, the crude product was precipitated with acetone and dissolved with cyclohexane for two cycles. Finally, the precipitation was redispersed in cyclohexane for further experiments.

### 2.5. Ligand Exchange to Prepare PEGylated $\text{Fe}_3\text{O}_4$ -Mal Nanoparticles

A total of 100 mg DP-PEG-Mal was dissolved in 4 mL THF containing 10 mg  $\text{Fe}_3\text{O}_4$  nanoparticles and stirred at  $60 \text{ }^\circ\text{C}$  for 24 h. Then, the solution was precipitated by adding cyclohexane and dissolved in THF afterward. After 2 cycles of purification, the precipitation was dried under a vacuum and dispersed in water. The aqueous solution was then ultrafiltrated four times with a 30 kDa MWCO centrifugal filter.

### 2.6. Preparation of $\text{Fe}_3\text{O}_4$ -Met-Cy5.5 and $\text{Fe}_3\text{O}_4$ -Cys-Cy5.5 Nanoprobosc

Met (0.25 mg,  $0.9 \text{ } \mu\text{mol}$ ) dissolving in DMSO or Cys (0.16 mg,  $0.9 \text{ } \mu\text{mol}$ ) dissolving in water were mixed, respectively, with the aqueous solution of tris(2-carboxyethyl) phosphine (80  $\mu\text{L}$ ,  $4 \text{ } \mu\text{mol}$ ). After being adjusted to neutrality by HEPES buffer ( $\text{pH} = 7.4$ , 1 M), the mixture was added to  $\text{Fe}_3\text{O}_4$ -Mal (containing 2.5 mg Fe) and oscillated for 12 h to obtain  $\text{Fe}_3\text{O}_4$ -Met or  $\text{Fe}_3\text{O}_4$ -Cys nanoprobosc.

Cy5.5-NHS (0.13 mg,  $0.18 \text{ } \mu\text{mol}$ ), dissolved in DMSO (65  $\mu\text{L}$ ), was added to  $\text{Fe}_3\text{O}_4$ -Met or  $\text{Fe}_3\text{O}_4$ -Cys (containing 2.5 mg Fe) and stirred for 12 h. The final product was dialyzed with Dialysis bags (MWCO: 12,000–14,000 Da) for 3 days and concentrated by a 30 kDa MWCO centrifugal filter.

### 2.7. Characterizations

Proton nuclear magnetic resonance ( $^1\text{H}$  NMR) spectra was obtained from Bruker Advance NEO 400 MHz. The morphology and size of the nanoparticles were taken with a high-resolution transmission electron microscope (Tenia G2 F20, FEI company, Hillsboro, CA, USA) at an acceleration voltage of 200 kV. The iron concentration was obtained by the 1,10-phenanthroline spectrophotometric method, after the resulting nanoparticles were eroded with the concentrated hydrochloric acid. The hydrodynamic size and zeta potential of nanoprobe were measured by Malvern Zetasizer Nano ZS90. Ultraviolet–visible absorption spectra were performed on the Persee dual-beam UV–Vis spectrophotometer. Fluorescence spectra were recorded by a steady-state/lifetime spectrofluorometer (FLS 980, Edinburgh Instruments, Livingston, Scotland). The relaxivity measurements were obtained by a 3 T animal MRI scanner (MRS 3000, MR Solution, Guildford, UK).

## 3. Results and Discussion

### 3.1. Synthesis and Characterization of Hypoxia-Sensitive Ligand

Due to the unique hypoxia-sensitive characteristics, metronidazole derivatives have been commonly used for hypoxia-selective prodrugs and imaging probes [38–40]. Herein, through an amidation reaction of Boc-Cys(Trt)-OH and metronidazole, followed by a deprotection reaction, 2-amino-3-mercapto-N-(2-(2-methyl-5-nitro-1H-imidazol-1-yl)ethyl)propanamide (Met) was achieved as the hypoxia-sensitive ligand. The detailed synthesis route,  $^1\text{H}$  NMR, and mass spectrum of the resulting product are given in the Supporting Information (Scheme S1, Figures S1 and S2, respectively). Moreover, Cys which lacks specificity toward hypoxia, was used to serve as the control ligand.

### 3.2. Construction and Characterization of Hypoxia-Sensitive MRI Nanoprobes

The transmission electron microscopy (TEM) images and the corresponding particle size distribution of ultrasmall  $\text{Fe}_3\text{O}_4$  nanoparticles were provided in Figure S3a in the Supporting Information. Polyethylene glycol (PEG) polymers, bearing a diphosphate group at one end and maleimide at the other, were employed to render the prepared nanoparticles hydrophilic by replacing the native organic ligands of the hydrophobic  $\text{Fe}_3\text{O}_4$  nanoparticles. As shown in Figure 1a,b, the resulting maleimide functionalized nanoparticles ( $\text{Fe}_3\text{O}_4\text{-Mal}$ ) exhibited a uniform spherical shape, with a mean size of  $3.6 \pm 0.3$  nm. Subsequently, the Met or Cys ligands was conjugated to the  $\text{Fe}_3\text{O}_4\text{-Mal}$  nanoparticles by a click reaction taking place between the maleimide groups of nanoparticles and the thiol moieties of the ligands. Finally, the surfaces of the resulting products were further modified by Cy5.5-NHS ester to construct the final hypoxia-sensitive and non-sensitive nanoprobe, termed  $\text{Fe}_3\text{O}_4\text{-Met-Cy5.5}$  and  $\text{Fe}_3\text{O}_4\text{-Cys-Cy5.5}$ , respectively (Scheme S2). As displayed in Figure S3b,c, the surface modification processes did not alter the morphology and size distribution of the original nanoparticles, such that spherical particles with the size of  $3.7 \pm 0.4$  nm were prepared in both cases. The dynamic light scattering (DLS) measurement results given in Figure 1c show that both  $\text{Fe}_3\text{O}_4\text{-Met-Cy5.5}$  and  $\text{Fe}_3\text{O}_4\text{-Cys-Cy5.5}$  exhibit narrow hydrodynamic size distribution profiles. However, the hydrodynamic size (Figure 1c) and zeta potential value (Figure 1d) of  $\text{Fe}_3\text{O}_4\text{-Met-Cy5.5}$  were slightly higher than those of  $\text{Fe}_3\text{O}_4\text{-Cys-Cy5.5}$ , which might be caused by the modification of the metronidazole groups. Anyway, the emergence of Cy5.5 characteristic absorption and emission peaks in the corresponding spectra (Figure 1e,f) of the resultant nanoprobe confirmed that two ligands and the dye molecules have successfully conjugated to the surface of the nanoprobe. Through ultraviolet–visible spectroscopy, the number of Cy5.5 moieties was estimated to be 4 on each nanoparticle.

To evaluate the colloidal stability, the prepared nanoprobe were incubated in water or PBS for up to 120 h, and the hydrodynamic sizes were monitored by DLS. The results shown in Figures 1g and S4a exhibited negligible change, which translated into the perfect colloidal stability of the nanoprobe. Subsequently, the relaxation measurements were performed under 3 T to assess the imaging performances of the prepared nanoprobe. As

shown in Figure S4b,c, increasing the concentration caused the signal intensity to increase under  $T_1$ -weighted mode and decrease under  $T_2$ -weighted mode, respectively. Through linear regression fitting of the experimental relaxation rates, as shown in Figure 1h, the longitudinal relaxivity ( $r_1$ ) of  $\text{Fe}_3\text{O}_4$ -Met-Cy5.5 and  $\text{Fe}_3\text{O}_4$ -Cys-Cy5.5 were calculated to be  $5.6 \text{ mM}^{-1} \text{ s}^{-1}$  and  $5.5 \text{ mM}^{-1} \text{ s}^{-1}$ , respectively. Similarly, as illustrated in Figure 1i, the transverse relaxivity ( $r_2$ ) values of  $31.0 \text{ mM}^{-1} \text{ s}^{-1}$  and  $27.0 \text{ mM}^{-1} \text{ s}^{-1}$  were measured for the hypoxia sensitive and non-sensitive probes, respectively. The high  $r_1$  value and the low  $r_2/r_1$  ratio suggested that both of the prepared nanoprobcs exhibited great relaxation performance and can be employed as promising contrast agents for  $T_1$ -weighted MRI.

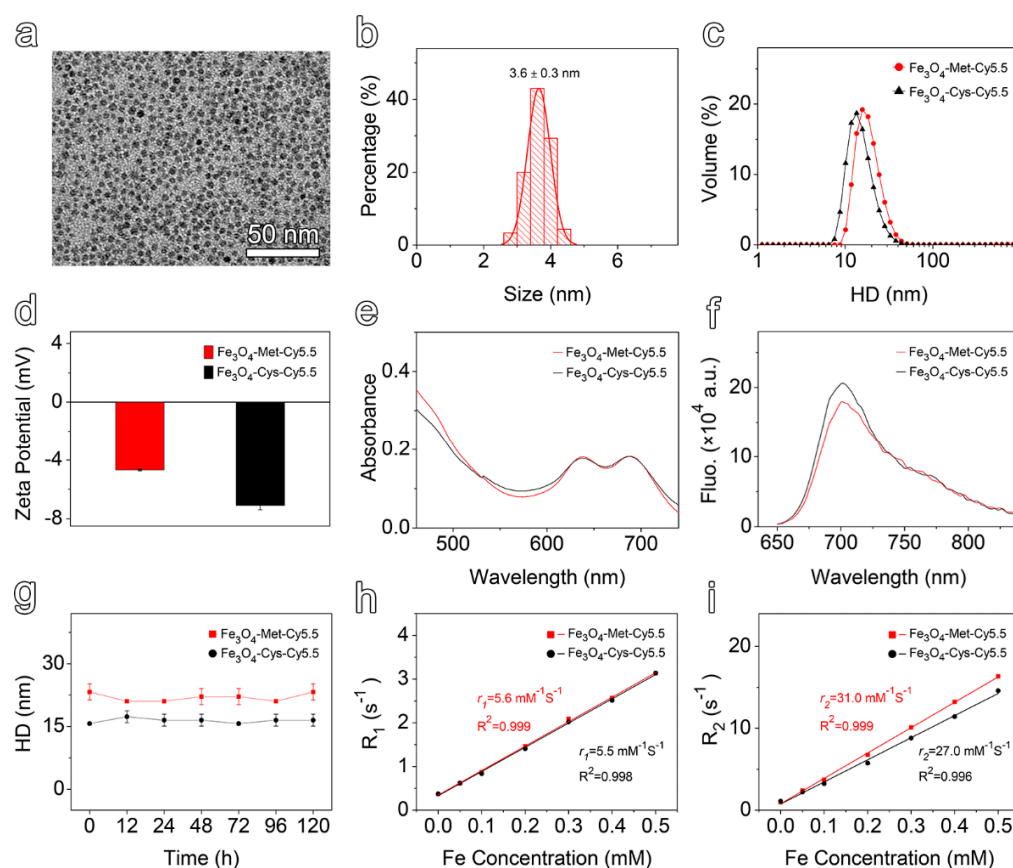


**Figure 1.** (a) TEM image and (b) size distribution of PEGylated  $\text{Fe}_3\text{O}_4$ -Mal nanoparticles. (c) Hydrodynamic size distribution and (d) zeta potential values of  $\text{Fe}_3\text{O}_4$ -Met-Cy5.5 and  $\text{Fe}_3\text{O}_4$ -Cys-Cy5.5. (e) Ultraviolet–visible absorption spectra of  $\text{Fe}_3\text{O}_4$ -Met-Cy5.5 and  $\text{Fe}_3\text{O}_4$ -Cys-Cy5.5, with a Fe concentration of  $50 \mu\text{g mL}^{-1}$ . (f) Fluorescence spectra of  $\text{Fe}_3\text{O}_4$ -Met-Cy5.5 and  $\text{Fe}_3\text{O}_4$ -Cys-Cy5.5, with a Fe concentration of  $50 \mu\text{g mL}^{-1}$  acquired at 705 nm upon excitation at 635 nm. (g) The hydrodynamic size variation of  $\text{Fe}_3\text{O}_4$ -Met-Cy5.5 and  $\text{Fe}_3\text{O}_4$ -Cys-Cy5.5 incubated in PBS for 120 h. Linear regression fitting of the longitudinal (h) and transverse (i) relaxivities of  $\text{Fe}_3\text{O}_4$ -Met-Cy5.5 and  $\text{Fe}_3\text{O}_4$ -Cys-Cy5.5 for extracting  $r_1$  and  $r_2$ .

### 3.3. In Vitro Specificity and Cytotoxicity of Hypoxia-Sensitive MRI Nanoprobcs

To investigate the efficacy of the prepared nanoprobcs in detecting hypoxic environments, MCF-7 cells with different hypoxic states were first obtained by incubating the cells under different oxygen concentrations for 12 h. Then, the expression of HIF-1 $\alpha$  was evaluated by Western Blot assays. As shown in Figure 2a,b, it was verified that the cells cultured in 3% and 1%  $\text{O}_2$  could establish hypoxic cell models for further experiments. Anyway, the protein expression values for the cells cultured under 1% and 3%  $\text{O}_2$  were 2.9 and 2.2 times higher than that of 21%, respectively.

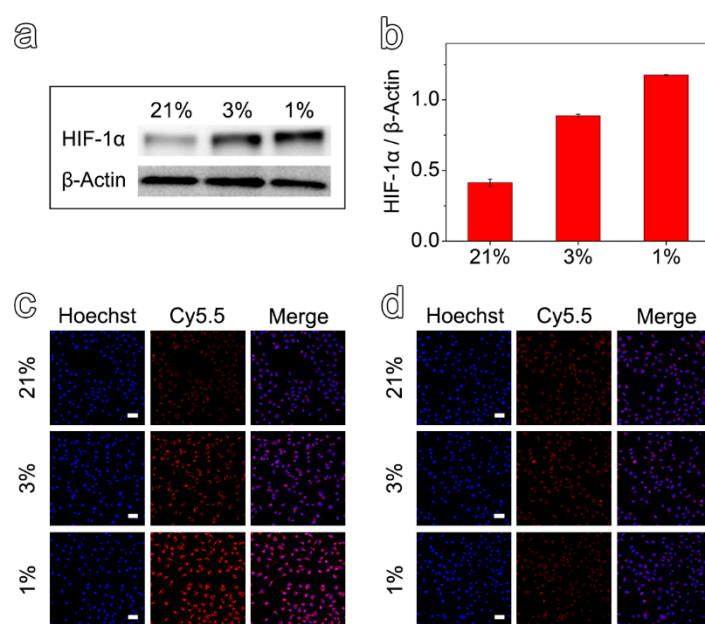


**Figure 2.** (a) Expression of HIF-1 $\alpha$  protein in MCF-7 cells incubated under the oxygen concentrations of 1%, 3%, and 21% for 12 h. (b) Semi-quantitative analysis of relative expression of HIF-1 $\alpha$  protein at different oxygen concentrations. Confocal fluorescence images of MCF-7 cells after incubation with Fe<sub>3</sub>O<sub>4</sub>-Met-Cy5.5 (c) or Fe<sub>3</sub>O<sub>4</sub>-Cys-Cy5.5 (d) at different oxygen concentrations (scale bar represents 50  $\mu$ m).

After demonstrating the different hypoxic states, the Fe<sub>3</sub>O<sub>4</sub>-Met-Cy5.5 and Fe<sub>3</sub>O<sub>4</sub>-Cys-Cy5.5 nanoprobe were incubated with hypoxic and normoxic cell models and observed by a confocal laser scanning microscope. Comparing the cells incubated with the two nanoprobe at the same hypoxia level (1% or 3% O<sub>2</sub>), the cellular accumulation of Fe<sub>3</sub>O<sub>4</sub>-Met-Cy5.5 was much higher than that of Fe<sub>3</sub>O<sub>4</sub>-Cys-Cy5.5 (Figure 2c,d). On the other hand, evaluating the cells incubated under three oxygen concentrations revealed that the cellular uptake of Fe<sub>3</sub>O<sub>4</sub>-Met-Cy5.5 increased in response to the decrease in the oxygen level. On the contrary, no apparent variation in cellular accumulation could be identified for the cells incubated with Fe<sub>3</sub>O<sub>4</sub>-Cys-Cy5.5. Particularly, as shown in Figure S5, the average fluorescence intensity arising from the Fe<sub>3</sub>O<sub>4</sub>-Met-Cy5.5 group under the oxygen concentrations of 1% and 3% were 2.8 and 1.6 times higher than that under 21% O<sub>2</sub>, respectively. It was noticed that the fluorescence enhancement of the Fe<sub>3</sub>O<sub>4</sub>-Met-Cy5.5 group was well-consistent with the increase of its HIF-1 $\alpha$  expression under a more severe state of hypoxia (1% O<sub>2</sub>). To further prove that the Fe<sub>3</sub>O<sub>4</sub>-Met-Cy5.5 probe has more uptake in a hypoxic environment, the nanoprobe were incubated with cells treated with hypoxia (1% O<sub>2</sub>) or normoxia (21% O<sub>2</sub>) for 12 h, and then followed by Prussian blue staining. As shown in Figure S6, more blue substances appeared in the cells of Fe<sub>3</sub>O<sub>4</sub>-Met-Cy5.5 group under 1% O<sub>2</sub>. These observations further confirmed that the Fe<sub>3</sub>O<sub>4</sub>-Met-Cy5.5 probe is sensitive to hypoxia cells, especially under severe hypoxia. The main reason is the accumulation and retention effect caused by the combination of metronidazole moieties and macromolecules in the hypoxic environment.

In comparison with the 2D cell model, the 3D multicellular spheres, which are better in line with the growth state of living cells *in vivo*, have been widely used in drug evaluation [41,42]. In addition, it has been reported that, for the multicellular spheres larger than 200  $\mu$ m in diameter, the conditions of hypoxia and necrosis might be induced due to the lack of nutrition supply [43]. Herein, the spheres with approximate diameters of 300  $\mu$ m were selected to be incubated with Fe<sub>3</sub>O<sub>4</sub>-Met-Cy5.5 and Fe<sub>3</sub>O<sub>4</sub>-Cys-Cy5.5 for 6 h. The representative slice images of multicellular spheres, obtained by a confocal laser scanning microscope, are given in Figure 3a, together with the quantified fluorescence

intensity results shown in Figure 3b. It is easily noticeable that the fluorescence signal of the multicellular spheres incubated with  $\text{Fe}_3\text{O}_4\text{-Met-Cy5.5}$  was stronger than that of the control group, especially in hypoxic inner areas. Furthermore, the intensity spectra close to the interior (100 to 200  $\mu\text{m}$ ) were integrated. It was found that the fluorescence intensity of the  $\text{Fe}_3\text{O}_4\text{-Met-Cy5.5}$  group was 2.1 times higher than that of  $\text{Fe}_3\text{O}_4\text{-Cys-Cy5.5}$ . The results proved that the  $\text{Fe}_3\text{O}_4\text{-Met-Cy5.5}$  probe also had a superior ability to be retained in the hypoxic regions of 3D multicellular spheres.

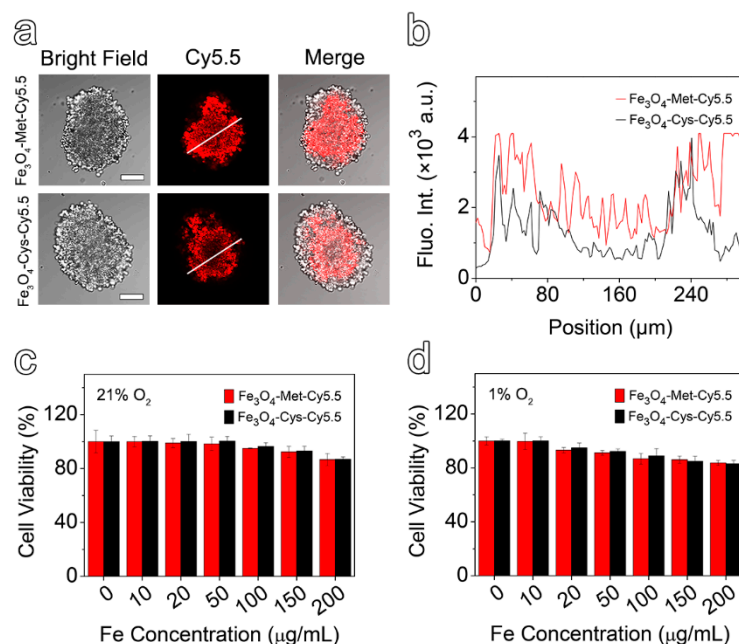


**Figure 3.** (a) The bright field and fluorescence images of multicellular spheres in the profile of 50  $\mu\text{m}$  from the maximum cross-section (scale bar represents 100  $\mu\text{m}$ ). (b) The relative fluorescence intensity distribution, along with the white line drawn on the fluorescence images. MCF-7 cells viabilities by CCK-8 assay after incubating with varied concentrations of  $\text{Fe}_3\text{O}_4\text{-Cys-Cy5.5}$  or  $\text{Fe}_3\text{O}_4\text{-Met-Cy5.5}$  under 21% (c) and 1%  $\text{O}_2$  (d).

To evaluate the cytotoxicity of  $\text{Fe}_3\text{O}_4\text{-Met-Cy5.5}$  and  $\text{Fe}_3\text{O}_4\text{-Cys-Cy5.5}$ , the standard cell counting kit 8 (CCK-8) assays were performed based on the proliferation of MCF-7 cells under 21% and 1%  $\text{O}_2$ . As depicted in Figure 3c,d, the viability values of the cells incubated with nanoprobe containing up to 200  $\mu\text{g mL}^{-1}$  of Fe were higher than 80%, regardless of the  $\text{O}_2$  concentration. These results suggested that both nanoprobe exhibited low cytotoxicity under both normoxic and hypoxic conditions and can be applied to *in vivo* imaging experiments.

### 3.4. *In Vivo* $T_1$ -Weighted MRI of Tumors

Based on the excellent hypoxia sensitivity *in vitro*, the nanoprobe were further intravenously injected into MCF-7 tumor-bearing mice (5.6 mg Fe  $\text{kg}^{-1}$  bodyweight) to explore the ability to detect hypoxia *in vivo* via MRI. The  $T_1$ -weighted MR images at different time points before (pre) and post-injection (2 h, 4 h, 6 h, 12 h, 24 h) were collected by 3 T MRI apparatus. The results in Figure 4a displayed an obvious brightening trend in the signal arising from the tumor site for both groups and up to 6 h post-injection. However, from 6 to 24 h after injection, a decreasing signal tendency was identified for both groups. Furthermore, the normalized ratio of signal intensity arising from the tumor site to that of normal muscle (T/N) in Figures 4a and S7 clearly exhibited that  $\text{Fe}_3\text{O}_4\text{-Met-Cy5.5}$  could provide a higher contrast than that of  $\text{Fe}_3\text{O}_4\text{-Cys-Cy5.5}$  (1.39 vs. 1.18 at 6 h post-injection). Anyway, the trend of the MRI signals in the two groups had statistically significant differences at 2, 4, 6, and 12 h post-injection (Figure S8a). Based on the above results, the ability



of  $\text{Fe}_3\text{O}_4\text{-Met-Cy5.5}$  and  $\text{Fe}_3\text{O}_4\text{-Cys-Cy5.5}$  to target the tumors through the EPR effect can presumably be considered similar, due to their similar sizes and surface modifications. Therefore, this higher tumor contrast was assumed to originate from the hypoxic condition of the tumor, which might lie in the specific accumulation of metronidazole moieties. This conjecture is reasonable as the central area of the tumor site in Figure 4a, which preferred a hypoxic state, due to the limited oxygen supply capacity, and was visibly brighter than the surrounding region of the tumor treated with  $\text{Fe}_3\text{O}_4\text{-Met-Cy5.5}$ . To verify this assumption, the tumors were harvested and subjected to H&E and immunofluorescence staining of the HIF-1 $\alpha$  antibody. As illustrated in Figure 4b,c, areas of tumor necrosis in H&E staining and hypoxic regions in HIF-1 $\alpha$  staining were identified for both groups. More importantly, the distribution of the red fluorescence of HIF-1 $\alpha$ , given in Figure 4b, was generally consistent with the brightening area of  $\text{Fe}_3\text{O}_4\text{-Met-Cy5.5}$ -treated group, verifying that our previous assumption was valid. In addition, Prussian blue staining of the hypoxic regions from the adjacent slices showed that both nanoprobe still had retention in the tumor regions after injection for 24 h (Figure 4d,e).

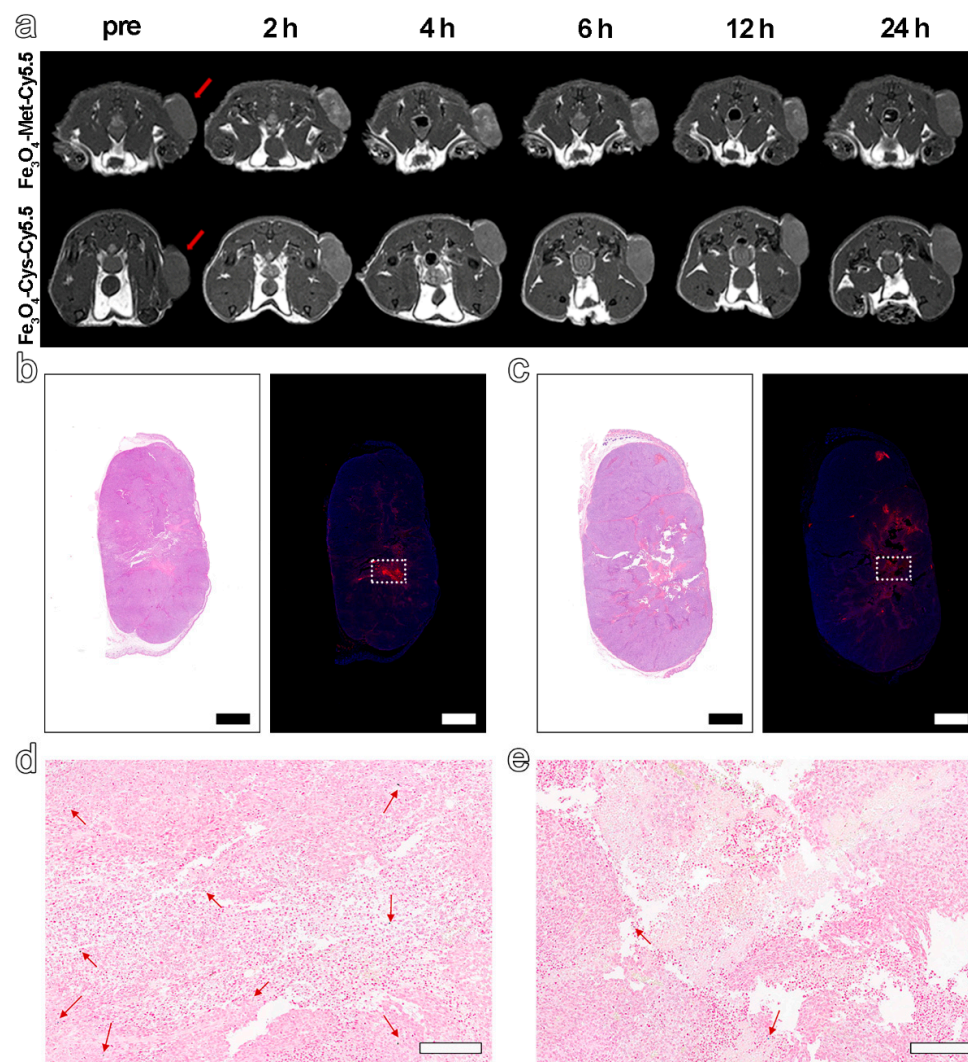


**Figure 4.** (a)  $T_1$ -weighted MRI of tumor-bearing mice within 24 h, before and after injection with  $\text{Fe}_3\text{O}_4\text{-Met-Cy5.5}$  or  $\text{Fe}_3\text{O}_4\text{-Cys-Cy5.5}$ . H&E staining (left) and immunofluorescence staining (right) for tumors of mice injected with  $\text{Fe}_3\text{O}_4\text{-Met-Cy5.5}$  (b) or  $\text{Fe}_3\text{O}_4\text{-Cys-Cy5.5}$  (c) (scale bars represent 1000  $\mu\text{m}$ ). Prussian blue staining of hypoxic area (dashed area on immunofluorescence staining images) in the tumors of mice treated with  $\text{Fe}_3\text{O}_4\text{-Met-Cy5.5}$  (d) or  $\text{Fe}_3\text{O}_4\text{-Cys-Cy5.5}$  (e) (scale bars represent 200  $\mu\text{m}$ ).

As the hypoxic areas in tumors may change slightly over time, the MRI was scanned again with the termination at the highest signal value (6 h) to further explore the ability of  $\text{Fe}_3\text{O}_4\text{-Met-Cy5.5}$  to visualize hypoxia distribution. As expected, we found a highly brightening contrast again in the central region of the tumor treated with  $\text{Fe}_3\text{O}_4\text{-Met-Cy5.5}$  (Figure 5a), and its signal value at 6 h was 1.40-fold higher than that of Pre (Figure 5b). However, the brightening effect was much weaker in the control group, and its signal value was only a 1.14-fold enhancement. As shown in Figure 5c,d, there were obvious positive areas in the center of the tumor, and the positive areas in the  $\text{Fe}_3\text{O}_4\text{-Met-Cy5.5}$  group were well-consistent with the signal-enhanced regions in the MRI images at 6 h. In addition, the expression of HIF-1 $\alpha$  in the central areas was significantly stronger than that of the surrounding less-hypoxic areas (Figure S8b). The above results indicated that the  $\text{Fe}_3\text{O}_4\text{-Met-Cy5.5}$  probe can achieve  $T_1$ -weighted MRI of hypoxic areas in tumors. Moreover, Prussian blue staining results demonstrated that the number of blue spots for the tumor treated with  $\text{Fe}_3\text{O}_4\text{-Met-Cy5.5}$  was significantly larger than that of the control group (Figure 5e,f), further proving the higher accumulation and retention of  $\text{Fe}_3\text{O}_4\text{-Met-Cy5.5}$  in hypoxic tumors. Anyway, the H&E staining (Figure S9) of both groups showed no obvious pathological symptoms of inflammation, cell edema, and necrosis in the tissues of tumor-bearing mice, indicating the biosafety of the two nanoprobres at the dosage of  $5.6 \text{ mg Fe kg}^{-1}$ .

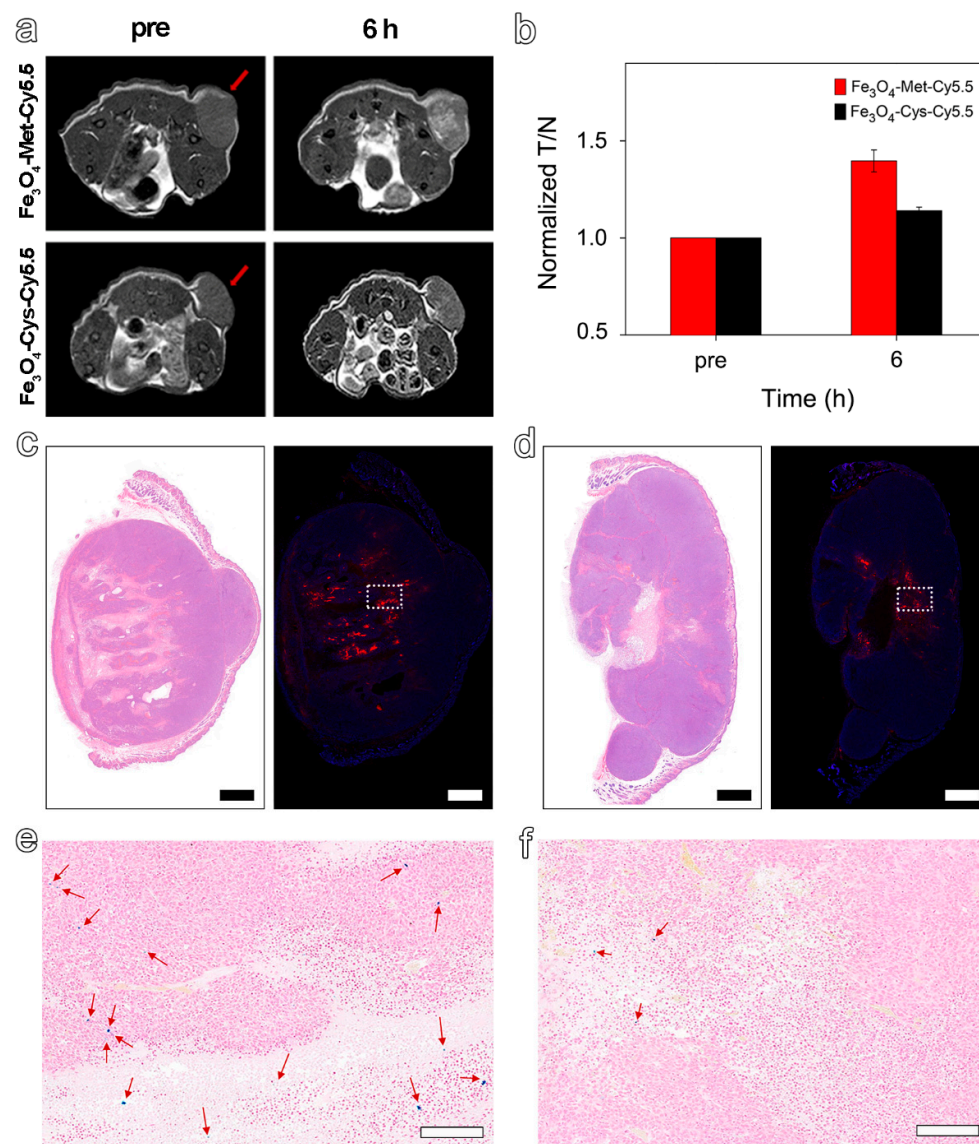


**Figure 5.** (a)  $T_1$ -weighted MRI of tumor-bearing mice before (pre) and 6 h post-injection of  $\text{Fe}_3\text{O}_4\text{-Met-}$

Cy5.5 or Fe<sub>3</sub>O<sub>4</sub>-Cys-Cy5.5. (b) The MRI signals at the time before (pre) and after (6 h) injection of Fe<sub>3</sub>O<sub>4</sub>-Met-Cy5.5 or Fe<sub>3</sub>O<sub>4</sub>-Cys-Cy5.5. H&E staining (left) and immunofluorescence staining (right) for tumors of mice injected with Fe<sub>3</sub>O<sub>4</sub>-Met-Cy5.5 (c) or Fe<sub>3</sub>O<sub>4</sub>-Cys-Cy5.5 (d) (scale bars represent 1000 μm). Prussian blue staining of hypoxic area (dashed area on immunofluorescence staining images) in the tumors of mice treated with Fe<sub>3</sub>O<sub>4</sub>-Met-Cy5.5 (e) or Fe<sub>3</sub>O<sub>4</sub>-Cys-Cy5.5 (f) (scale bars represent 200 μm).

#### 4. Conclusions

In conclusion, we have successfully constructed an ultrasmall Fe<sub>3</sub>O<sub>4</sub>-based T<sub>1</sub>-weighted MRI probe with outstanding relaxivity performance, biocompatibility, and hypoxia specificity. The in vitro cell experiments showed that the accumulation of Fe<sub>3</sub>O<sub>4</sub>-Met-Cy5.5 under hypoxic condition was consistent with the increase of HIF-1α expression level, which proved the excellent hypoxia sensitivity of the resultant nanoprobe. After being intravenously injected into the tumor-bearing mice model, the significantly enhanced signal contrast in the tumors' interior regions confirmed the hypoxia sensitivity of the Fe<sub>3</sub>O<sub>4</sub>-Met-Cy5.5 in vivo. Anyway, the comparison between the brightening MRI and hypoxia immunofluorescence images further demonstrated the feasibility of the resultant nanoprobe for depicting the hypoxia area in tumors. Therefore, this work not only exhibits the potential of ultrasmall Fe<sub>3</sub>O<sub>4</sub> in tumor diagnostic imaging as T<sub>1</sub>-weighted MRI contrast agents but also provides a valuable reference for hypoxia imaging probes in the future.

**Supplementary Materials:** The following supporting information can be downloaded at: <https://www.mdpi.com/article/10.3390/molecules27206929/s1>, Scheme S1: Synthetic route of hypoxia-sensitive ligand (Met), Scheme S2: Synthetic route of Fe<sub>3</sub>O<sub>4</sub>-Met-Cy5.5 and Fe<sub>3</sub>O<sub>4</sub>-Cys-Cy5.5, Figure S1: <sup>1</sup>H NMR spectrum of hypoxia-sensitive ligand (Met), Figure S2: Mass spectrum of hypoxia-sensitive ligand (Met), Figure S3: TEM images and the size distributions of Fe<sub>3</sub>O<sub>4</sub> (a), Fe<sub>3</sub>O<sub>4</sub>-Met-Cy5.5 (b), and Fe<sub>3</sub>O<sub>4</sub>-Cys-Cy5.5 (c) nanoparticles, Figure S4: The evaluation of colloid stability for Fe<sub>3</sub>O<sub>4</sub>-Met-Cy5.5 and Fe<sub>3</sub>O<sub>4</sub>-Cys-Cy5.5 stored in water for 120 h (a). T<sub>1</sub>-weighted (b) and T<sub>2</sub>-weighted (c) MR images of the Fe<sub>3</sub>O<sub>4</sub>-Met-Cy5.5 and Fe<sub>3</sub>O<sub>4</sub>-Cys-Cy5.5 at different Fe concentrations (0, 0.05, 0.1, 0.2, 0.3, 0.4, 0.5 mM), Figure S5: Semi-quantitative analysis of MCF-7 cells fluorescence imaging under three oxygen concentrations, Figure S6: Prussian blue staining of MCF-7 cells incubated with Fe<sub>3</sub>O<sub>4</sub>-Met-Cy5.5 or Fe<sub>3</sub>O<sub>4</sub>-Cys-Cy5.5 probe at different oxygen concentrations for 12 h (scale bar represents 10 μm). Figure S7: T<sub>1</sub>-weighted MRI of two additional tumor-bearing mice for each group within 24 h, before and after injection with Fe<sub>3</sub>O<sub>4</sub>-Met-Cy5.5 or Fe<sub>3</sub>O<sub>4</sub>-Cys-Cy5.5, Figure S8: (a) The trend of MRI signal at different time points in tumors injected with Fe<sub>3</sub>O<sub>4</sub>-Met-Cy5.5 or Fe<sub>3</sub>O<sub>4</sub>-Cys-Cy5.5. (b) Semi-quantitative analysis of HIF-1α expression of the less-hypoxic and hypoxic regions in tumors treated with Fe<sub>3</sub>O<sub>4</sub>-Met-Cy5.5 or Fe<sub>3</sub>O<sub>4</sub>-Cys-Cy5.5, Figure S9: H&E staining of organ tissue (heart, liver, spleen, lung, and kidney) from mice harvested at 24 h after the injection of Fe<sub>3</sub>O<sub>4</sub>-Met-Cy5.5 or Fe<sub>3</sub>O<sub>4</sub>-Cys-Cy5.5 (scale bar represents 100 μm). Ref. [44] appears in Supplementary Materials.

**Author Contributions:** Conceptualization, L.Y. and J.Z. (Jianfeng Zeng); methodology, L.Y. and L.C.; investigation, L.Y., J.G. and L.Z.; writing—original draft preparation, L.Y. and M.J.A.; writing—review and editing, D.K., D.Z., C.L., S.W. and J.Z. (Jianfeng Zeng); supervision, J.Z. (Jian Zhong), J.Z. (Jianfeng Zeng), R.H.S. and M.G.; funding acquisition, J.Z. (Jianfeng Zeng) and M.G. All authors have read and agreed to the published version of the manuscript.

**Funding:** This research was funded by the National Key Research and Development Program of China (2018YFA0208800), the National Natural Science Foundation of China (82130059, 82172003, 81720108024), the Nature Science Foundation of Jiangsu Higher Education Institutions of China (20KJA150006), the Natural Science Foundation of Jiangsu Province (BK20191418), the Suzhou Key Industry Technology Innovation Projects (SYG202036), and the Priority Academic Program Development of Jiangsu Higher Education Institutions (PAPD).

**Institutional Review Board Statement:** The study was conducted according to the guidelines of the Declaration of Helsinki and approved by Soochow University Laboratory Animal Center.

**Informed Consent Statement:** Not applicable.

**Data Availability Statement:** Data are contained within the article or supplementary material.

**Acknowledgments:** The authors thank for Suzhou Vivoid Biotechnology Co., Ltd., Suzhou, China, which holds stamping technology for cell spheroid formation in the agarose sheet.

**Conflicts of Interest:** The authors declare no competing interest.

**Sample Availability:** Samples of the compounds are not available from the authors.

## References

1. Gilkes, D.M.; Semenza, G.L.; Wirtz, D. Hypoxia and the Extracellular Matrix: Drivers of Tumour Metastasis. *Nat. Rev. Cancer* **2014**, *14*, 430–439. [[CrossRef](#)]
2. Vaupel, P.; Briest, S.; Hockel, M. Hypoxia in Breast Cancer: Pathogenesis, Characterization and Biological/Therapeutic Implications. *Wien. Med. Wochenschr.* **2002**, *152*, 334–342. [[CrossRef](#)] [[PubMed](#)]
3. Vaupel, P.; Harrison, L. Tumor Hypoxia: Causative Factors, Compensatory Mechanisms, and Cellular Response. *Oncologist* **2004**, *9* (Suppl. S5), 4–9. [[CrossRef](#)] [[PubMed](#)]
4. Jubb, A.M.; Buffa, F.M.; Harris, A.L. Assessment of Tumour Hypoxia for Prediction of Response to Therapy and Cancer Prognosis. *J. Cell. Mol. Med.* **2010**, *14*, 18–29. [[CrossRef](#)]
5. Ma, T.; Zhang, P.; Hou, Y.; Ning, H.; Wang, Z.; Huang, J.; Gao, M. "Smart" Nanoprobes for Visualization of Tumor Microenvironments. *Adv. Healthc. Mater.* **2018**, *7*, e1800391. [[CrossRef](#)] [[PubMed](#)]
6. Phung, C.D.; Tran, T.H.; Pham, L.M.; Nguyen, H.T.; Jeong, J.H.; Yong, C.S.; Kim, J.O. Current Developments in Nanotechnology for Improved Cancer Treatment, Focusing on Tumor Hypoxia. *J. Control. Release* **2020**, *324*, 413–429. [[CrossRef](#)] [[PubMed](#)]
7. Koukourakis, M.I.; Giatromanolaki, A.; Danielidis, V.; Sivridis, E. Hypoxia Inducible Factor (HIF1 alpha and HIF2 alpha) and Carbonic Anhydrase 9 (CA9) Expression and Response of Head-neck Cancer to Hypofractionated and Accelerated Radiotherapy. *Int. J. Radiat. Biol.* **2008**, *84*, 47–52. [[CrossRef](#)]
8. Rey, S.; Schito, L.; Koritzinsky, M.; Wouters, B.G. Molecular Targeting of Hypoxia in Radiotherapy. *Adv. Drug Deliv. Rev.* **2017**, *109*, 45–62. [[CrossRef](#)] [[PubMed](#)]
9. Vaupel, P. The Role of Hypoxia-Induced Factors in Tumor Progression. *Oncologist* **2004**, *9*, 10–17. [[CrossRef](#)] [[PubMed](#)]
10. Rankin, E.B.; Giaccia, A.J. Hypoxic Control of Metastasis. *Science* **2016**, *352*, 175–180. [[CrossRef](#)]
11. Vaupel, P.; Schlenger, K.; Knoop, C.; Hockel, M. Oxygenation of Human Tumors: Evaluation of Tissue Oxygen Distribution in Breast Cancers by Computerized O<sub>2</sub> Tension Measurements. *Cancer Res.* **1991**, *51*, 3316–3322.
12. Olive, P.L.; Banath, J.P.; Aquino-Parsons, C. Measuring Hypoxia in Solid Tumours—Is there a gold standard? *Acta Oncol.* **2001**, *40*, 917–923. [[PubMed](#)]
13. Sun, X.; Niu, G.; Chan, N.; Shen, B.; Chen, X. Tumor Hypoxia Imaging. *Mol. Imaging Biol.* **2011**, *13*, 399–410. [[CrossRef](#)] [[PubMed](#)]
14. Liu, J.N.; Bu, W.; Shi, J. Chemical Design and Synthesis of Functionalized Probes for Imaging and Treating Tumor Hypoxia. *Chem. Rev.* **2017**, *117*, 6160–6224. [[CrossRef](#)] [[PubMed](#)]
15. Cheng, M.H.Y.; Mo, Y.; Zheng, G. Nano versus Molecular: Optical Imaging Approaches to Detect and Monitor Tumor Hypoxia. *Adv. Healthc. Mater.* **2021**, *10*, e2001549. [[CrossRef](#)]
16. Nan, Y.X.; Zhou, Q.L.; Zhao, W.J.; Lu, Y.B.; Xu, W.J. In Vivo Imaging of Hypoxia Generation Stimulated by Testosterone Using a Micelle-Based Near-Infrared Fluorescent Probe. *Sens. Actuators B Chem.* **2019**, *288*, 543–551. [[CrossRef](#)]
17. Berezin, M.Y.; Achilefu, S. Fluorescence Lifetime Measurements and Biological Imaging. *Chem. Rev.* **2010**, *110*, 2641–2684. [[CrossRef](#)]
18. Yoshihara, K.; Takagi, K.; Son, A.; Kurihara, R.; Tanabe, K. Aggregate Formation of Oligonucleotides that Assist Molecular Imaging for Tracking of the Oxygen Status in Tumor Tissue. *ChemBioChem* **2017**, *18*, 1650–1658. [[CrossRef](#)] [[PubMed](#)]
19. Zheng, X.C.; Mao, H.; Huo, D.; Wu, W.; Liu, B.R.; Jiang, X.Q. Successively Activatable Ultrasensitive Probe for Imaging Tumour Acidity and Hypoxia. *Nat. Biomed. Eng.* **2017**, *1*, 0057. [[CrossRef](#)]
20. Xiao, P.; Liu, C.; Ma, T.; Lu, X.; Jing, L.; Hou, Y.; Zhang, P.; Huang, G.; Gao, M. A Cyclodextrin-Hosted Ir(III) Complex for Ratiometric Mapping of Tumor Hypoxia In Vivo. *Adv. Sci.* **2021**, *8*, 2004044. [[CrossRef](#)]
21. Rajendran, J.G.; Wilson, D.C.; Conrad, E.U.; Peterson, L.M.; Bruckner, J.D.; Rasey, J.S.; Chin, L.K.; Hofstrand, P.D.; Grierson, J.R.; Eary, J.F.; et al. <sup>18</sup>F-FMISO and <sup>18</sup>F-FDG PET Imaging in Soft Tissue Sarcomas: Correlation of Hypoxia, Metabolism and VEGF Expression. *Eur. J. Nucl. Med. Mol. Imaging* **2003**, *30*, 695–704. [[CrossRef](#)] [[PubMed](#)]
22. Halmos, G.B.; de Bruin, L.B.; Langendijk, J.A.; van der Laan, B.F.A.M.; Pruim, J.; Steenbakkers, R.J.H.M. Head and Neck Tumor Hypoxia Imaging by <sup>18</sup>F-Fluoroazomycin-araboside (<sup>18</sup>F-FAZA)-PET: A Review. *Clin. Nucl. Med.* **2014**, *39*, 44–48. [[CrossRef](#)]
23. Zegers, C.M.; van Elmpt, W.; Szardenings, K.; Kolb, H.; Waxman, A.; Subramaniam, R.M.; Moon, D.H.; Brunetti, J.C.; Srinivas, S.M.; Lambin, P.; et al. Repeatability of Hypoxia PET Imaging Using <sup>18</sup>F-HX4 in Lung and Head and Neck Cancer Patients: A Prospective Multicenter Trial. *Eur. J. Nucl. Med. Mol. Imaging* **2015**, *42*, 1840–1849. [[CrossRef](#)] [[PubMed](#)]
24. Pinto, S.M.; Tome, V.; Calvete, M.J.F.; Castro, M.M.C.A.; Toth, E.; Geraldes, C.F.G.C. Metal-Based Redox-Responsive MRI Contrast Agents. *Coord. Chem. Rev.* **2019**, *390*, 1–31. [[CrossRef](#)]
25. Hu, Y.; Mignani, S.; Majoral, J.P.; Shen, M.; Shi, X. Construction of Iron Oxide Nanoparticle-Based Hybrid Platforms for Tumor Imaging and Therapy. *Chem. Soc. Rev.* **2018**, *47*, 1874–1900. [[CrossRef](#)]

26. Filippi, M.; Nguyen, D.V.; Garello, F.; Perton, F.; Begin-Colin, S.; Felder-Flesch, D.; Power, L.; Scherberich, A. Metronidazole-Functionalized Iron Oxide Nanoparticles for Molecular Detection of Hypoxic Tissues. *Nanoscale* **2019**, *11*, 22559–22574. [[CrossRef](#)] [[PubMed](#)]
27. Zhou, H.; Guo, M.; Li, J.; Qin, F.; Wang, Y.; Liu, T.; Liu, J.; Sabet, Z.F.; Wang, Y.; Liu, Y.; et al. Hypoxia-Triggered Self-Assembly of Ultrasmall Iron Oxide Nanoparticles to Amplify the Imaging Signal of a Tumor. *J. Am. Chem. Soc.* **2021**, *143*, 1846–1853. [[CrossRef](#)] [[PubMed](#)]
28. Park, M.; Lee, N.; Choi, S.H.; An, K.; Yu, S.H.; Kim, J.H.; Kwon, S.H.; Kim, D.; Kim, H.; Baek, S.I.; et al. Large-Scale Synthesis of Ultrathin Manganese Oxide Nanoplates and Their Applications to  $T_1$  MRI Contrast Agents. *Chem. Mater.* **2011**, *23*, 3318–3324. [[CrossRef](#)]
29. Chen, C.; Ge, J.; Gao, Y.; Chen, L.; Cui, J.; Zeng, J.; Gao, M. Ultrasmall Superparamagnetic Iron Oxide Nanoparticles: A Next Generation Contrast Agent for Magnetic Resonance Imaging. *WIREs Nanomed. Nanobiotechnol.* **2022**, *14*, e1740. [[CrossRef](#)] [[PubMed](#)]
30. Sandiford, L.; Phinikaridou, A.; Protti, A.; Meszaros, L.K.; Cui, X.; Yan, Y.; Frodsham, G.; Williamson, P.A.; Gaddum, N.; Botnar, R.M.; et al. Bisphosphonate-Anchored PEGylation and Radiolabeling of Superparamagnetic Iron Oxide: Long-Circulating Nanoparticles for In Vivo Multimodal ( $T_1$  MRI-SPECT) Imaging. *ACS Nano* **2013**, *7*, 500–512. [[CrossRef](#)]
31. Jia, Z.; Song, L.; Zang, F.; Song, J.; Zhang, W.; Yan, C.; Xie, J.; Ma, Z.; Ma, M.; Teng, G.; et al. Active-Target  $T_1$ -Weighted MR Imaging of Tiny Hepatic Tumor via RGD Modified Ultra-Small  $Fe_3O_4$  Nanoparticles. *Theranostics* **2016**, *6*, 1780–1791. [[CrossRef](#)] [[PubMed](#)]
32. Lu, Y.; Xu, Y.J.; Zhang, G.B.; Ling, D.; Wang, M.Q.; Zhou, Y.; Wu, Y.D.; Wu, T.; Hackett, M.J.; Hyo Kim, B.; et al. Iron Oxide Nanoclusters for  $T_1$  Magnetic Resonance Imaging of Non-Human Primates. *Nat. Biomed. Eng.* **2017**, *1*, 637–643. [[CrossRef](#)]
33. Kim, M.H.; Son, H.Y.; Kim, G.Y.; Park, K.; Huh, Y.M.; Haam, S. Redoxable Heteronanocrystals Functioning Magnetic Relaxation Switch for Activatable  $T_1$  and  $T_2$  Dual-Mode Magnetic Resonance Imaging. *Biomaterials* **2016**, *101*, 121–130. [[CrossRef](#)] [[PubMed](#)]
34. Edwards, D.I. Nitroimidazole Drugs-Action and Resistance Mechanisms. I. Mechanisms of Action. *J. Antimicrob. Chemother.* **1993**, *31*, 9–20. [[CrossRef](#)]
35. Handley, M.G.; Medina, R.A.; Nagel, E.; Blower, P.J.; Southworth, R. PET Imaging of Cardiac Hypoxia: Opportunities and Challenges. *J. Mol. Cell. Cardiol.* **2011**, *51*, 640–650. [[CrossRef](#)]
36. Strauss, H.W.; Nunn, A.; Linder, K. Nitroimidazoles for Imaging Hypoxic Myocardium. *J. Nucl. Cardiol.* **1995**, *2*, 437–445. [[CrossRef](#)]
37. Jiao, M.X.; Zeng, J.F.; Jing, L.H.; Liu, C.Y.; Gao, M.Y. Flow Synthesis of Biocompatible  $Fe_3O_4$  Nanoparticles: Insight into the Effects of Residence Time, Fluid Velocity, and Tube Reactor Dimension on Particle Size Distribution. *Chem. Mater.* **2015**, *27*, 1299–1305. [[CrossRef](#)]
38. Mallia, M.B.; Mathur, A.; Subramanian, S.; Banerjee, S.; Sarma, H.D.; Venkatesh, M. A Novel [ $^{99m}Tc$ (triple bond) $N$ ] $^{2+}$  Complex of Metronidazole Xanthate as a Potential Agent for Targeting Hypoxia. *Bioorg. Med. Chem. Lett.* **2005**, *15*, 3398–3401. [[CrossRef](#)]
39. Lages, E.B.; de Freitas, M.B.; Goncalves, I.M.; Alves, R.J.; Vianna-Soares, C.D.; Ferreira, L.A.; de Oliveira, M.C.; de Oliveira, R.B. Evaluation of Antitumor Activity and Development of Solid Lipid Nanoparticles of Metronidazole Analogue. *J. Biomed. Nanotechnol.* **2013**, *9*, 1939–1944. [[CrossRef](#)] [[PubMed](#)]
40. Javani, S.; Barsbay, M.; Ghaffarlou, M.; Mousazadeh, N.; Mohammadi, A.; Mozafari, F.; Rezaeejam, H.; Nasehi, L.; Nosrati, H.; Kavetskiy, T.; et al. Metronidazole Conjugated Bismuth Sulfide Nanoparticles for Enhanced X-Ray Radiation Therapy. *J. Drug Deliv. Sci. Technol.* **2022**, *71*, 103336. [[CrossRef](#)]
41. Chen, S.; Zhong, Y.; Fan, W.; Xiang, J.; Wang, G.; Zhou, Q.; Wang, J.; Geng, Y.; Sun, R.; Zhang, Z.; et al. Enhanced Tumour Penetration and Prolonged Circulation in Blood of Polyzwitterion-Drug Conjugates with Cell-Membrane Affinity. *Nat. Biomed. Eng.* **2021**, *5*, 1019–1037. [[CrossRef](#)] [[PubMed](#)]
42. Wang, G.W.; Zhang, C.; Jiang, Y.F.; Song, Y.; Chen, J.F.; Sun, Y.; Li, Q.Y.; Zhou, Z.X.; Shen, Y.Q.; Huang, P.T. Ultrasonic Cavitation-Assisted and Acid-Activated Transcytosis of Liposomes for Universal Active Tumor Penetration. *Adv. Funct. Mater.* **2021**, *31*, 2102786. [[CrossRef](#)]
43. Lu, H.; Stenzel, M.H. Multicellular Tumor Spheroids (MCTS) as a 3D In Vitro Evaluation Tool of Nanoparticles. *Small* **2018**, *14*, e1702858. [[CrossRef](#)] [[PubMed](#)]
44. Guo, S.; Sun, D.; Ni, D.; Yu, M.; Qian, K.; Zhang, W.; Yang, Y.; Song, S.; Li, Y.; Xi, Z.; et al. Smart Tumor Microenvironment-Responsive Nanotheranostic Agent for Effective Cancer Therapy. *Adv. Funct. Mater.* **2020**, *30*, 2000486. [[CrossRef](#)]